

See discussions, stats, and author profiles for this publication at: <https://www.researchgate.net/publication/253337046>

Photo-Induced Heating of Nanoparticle Arrays.

ARTICLE *in* ACS NANO · JULY 2013

Impact Factor: 12.88 · DOI: 10.1021/nn401924n · Source: PubMed

CITATIONS

30

READS

76

7 AUTHORS, INCLUDING:



[Esteban Bermudez](#)

ICFO Institute of Photonic Sciences

18 PUBLICATIONS 613 CITATIONS

[SEE PROFILE](#)



[Romain Quidant](#)

ICFO Institute of Photonic Sciences

178 PUBLICATIONS 5,814 CITATIONS

[SEE PROFILE](#)



[Serge Monneret](#)

Aix-Marseille Université

132 PUBLICATIONS 719 CITATIONS

[SEE PROFILE](#)



[Julien Polleux](#)

Max Planck Institute of Biochemistry

36 PUBLICATIONS 2,551 CITATIONS

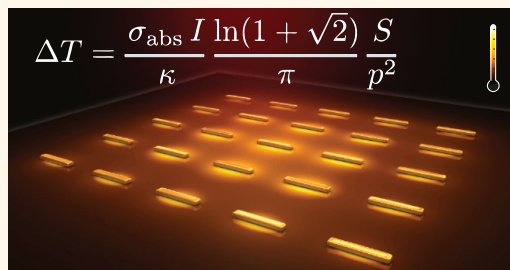
[SEE PROFILE](#)

Photoinduced Heating of Nanoparticle Arrays

Guillaume Baffou,^{†,*} Pascal Berto,[†] Esteban Bermúdez Ureña,[‡] Romain Quidant,^{*,§} Serge Monneret,[†] Julien Polleux,[⊥] and Hervé Rigneault[†]

[†]Aix Marseille Université, CNRS, Centrale Marseille, Institut Fresnel, UMR 7249, 13013 Marseille, France, [‡]ICFO-Institut de Ciències Fotòniques, Mediterranean Technology Park, 08860 Castelldefels (Barcelona), Spain, [§]ICREA-Institució Catalana de Recerca i Estudis Avançats, 08010 Barcelona, Spain, and [⊥]Department of Molecular Medicine, Max Planck Institute of Biochemistry, 82152 Martinsried, Germany

ABSTRACT The temperature distribution throughout arrays of illuminated metal nanoparticles is investigated numerically and experimentally. The two cases of continuous and femtosecond-pulsed illumination are addressed. In the case of continuous illumination, two distinct regimes are evidenced: a temperature confinement regime, where the temperature increase remains confined at the vicinity of each nanosource of heat, and a temperature delocalization regime, where the temperature is uniform throughout the whole nanoparticle assembly despite the heat sources' nanometric size. We show that the occurrence of one regime or another simply depends on the geometry of the nanoparticle distribution. In particular, we derived (i) simple expressions of dimensionless parameters aimed at predicting the degree of temperature confinement and (ii) analytical expressions aimed at estimating the actual temperature increase at the center of an assembly of nanoparticles under illumination, preventing heavy numerical simulations. All these theoretical results are supported by experimental measurements of the temperature distribution on regular arrays of gold nanoparticles under illumination. In the case of femtosecond-pulsed illumination, we explain the two conditions that must be fulfilled to observe a further enhanced temperature spatial confinement.



KEYWORDS: plasmonics · arrays · photothermal · temperature microscopy · wavefront sensing · femtosecond pulse

Metal nanoparticles (NPs), when illuminated at their plasmonic resonance, can turn into very efficient nanosources of heat due to enhanced light absorption.^{1–3} This simple behavior is the basis of numerous applications and promising achievements in nanotechnology, namely, for nanoscale control of temperature distribution,⁴ photothermal cancer therapy,^{5–7} nanosurgery,⁸ drug delivery,^{9–11} photothermal imaging,¹² photoacoustic imaging,¹³ phase transition,¹⁴ nanochemistry,^{15,16} and optofluidics.¹⁷

Using arrays of metal nanostructures offers the advantage of investigating nanoscale processes over a large quantity of equivalent systems at once, which substantially increases the signal-to-noise ratio. This past decade, many investigations of metal NP arrays have been reported, in research areas such as nanochemistry,¹⁶ biosensing,^{18,19} heat generation,²⁰ fluorescence enhancement,²¹ second-harmonic generation,²² surface-enhanced Raman scattering (SERS),^{23,24} and organic–inorganic optical coupling.²⁵

Experimentally, Govorov, Richardson, *et al.* have shown that, when illuminating a large amount of gold NPs dispersed in solution, the temperature profile throughout the system may no longer be localized around each NP due to some thermal collective effects.^{26,27} The temperature can become uniform throughout the NP assembly, although the size of the sources of heat is nanometric. While this situation is suited for applications such as photothermal cancer therapy, it is usually not favorable for nanoscale applications where a localized heating is desired.

Theoretically, numerical techniques have been recently developed to model the photothermal behavior (temperature and heat source density) of a single illuminated metal NP, either under continuous (CW) or pulsed illumination.^{4,28–30} However, when considering the heat generation from an assembly of NPs in close proximity, the problem becomes more complex, and it is usually too memory-consuming to mesh the whole system and carry out numerical

* Address correspondence to guillaume.baffou@fresnel.fr.

Received for review April 18, 2013 and accepted July 26, 2013.

Published online July 27, 2013
10.1021/nn401924n

© 2013 American Chemical Society

simulations. If the NP assembly consists of a periodic array of NPs, the periodicity makes the computation easier regarding the *optical* properties, since the problem can be reduced to the study of a single lattice unit cell. However, it does not make sense to compute the temperature distribution over a periodic array of NPs since the temperature increase generated by an infinite number of NPs is infinite, in any case. A finite number of NPs has to be specified in any computation in order to end up with a finite temperature increase. This feature makes any computation of the temperature generated by a large amount of photothermal nanosources intricate.

In this work, we investigate theoretically the properties of the temperature distribution throughout arbitrarily large metal NP assemblies. To simplify the discussion and easily derive the general trends, we consider *regular* distributions of NPs: one-dimensional (line) and two-dimensional (either square or hexagonal) lattices of NPs. In particular, we derive simple formulas to estimate the temperature increase achieved at the center of any lattice and the degree of temperature confinement. Indeed, two regimes are evidenced: a temperature confinement regime, where the temperature distribution is mostly confined at the vicinity of each NP, and a delocalization regime, where the temperature profile is smooth throughout the system despite of the nanometric nature of the heat sources. All these theoretical results are supported by temperature measurements on gold NPs using quadriwave lateral shearing interferometry.³¹ We finally explain how and to what extent a much higher spatial confinement can be achieved using femtosecond-pulsed optical heating.

RESULTS AND DISCUSSION

Theoretical Model. As mentioned above, many applications in plasmonics are based on the use of periodic arrays of identical metal NPs. Several experimental techniques have been developed to design such samples, *e.g.*, e-beam lithography, nanosphere lithography, or diblock copolymer micellar photolithography. Figure 1 shows some examples of typical periodic systems that can be fabricated using these techniques.

To model such systems, we shall consider in this work an assembly of N identical metal NPs deposited on a planar substrate. The dielectric permittivities of the NP, the surrounding medium, and the substrate are ε_{NP} , $\varepsilon = n^2$, and $\varepsilon_s = n_s^2$ and the thermal conductivities κ_{NP} , κ , and κ_s , respectively. The NPs are heated using a monochromatic light at the angular frequency $\omega = 2\pi c/\lambda$, c being the speed of light in vacuum. For the sake of clarity, the most important notations are gathered and defined in Table 1.

Anywhere in the system, the electric field reads $\mathbf{E}(\mathbf{r}, t) = \text{Re}(\mathbf{E}(\mathbf{r})e^{-i\omega t})$, where $\mathbf{E}(\mathbf{r})$ is its complex amplitude. We name $\mathbf{E}_0(\mathbf{r})$ the electric field amplitude of the illumination and $\mathbf{E}_j^{\text{ext}}$ the external electric field

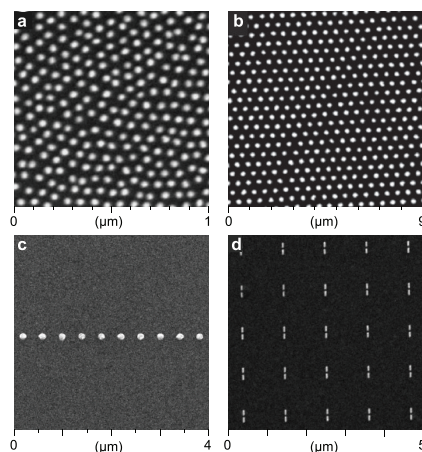


Figure 1. Examples of arrays of NPs observed by scanning electron microscopy (SEM). (a) Quasi-hexagonal array of gold NPs created by diblock copolymer micellar lithography. (b) Hexagonal array of gold NPs made by nanosphere lithography. (c) One-dimensional array of gold NPs made by e-beam lithography. (d) Periodic array of gold nanoantennas made by e-beam lithography.

TABLE 1. Notations Used in This Article

name	description	dimension
σ_{abs}	NP absorption cross section	m^2
λ	free space illumination wavelength	m
P	power of the illumination	W
I	irradiance of the illumination	W m^{-2}
f	pulsation rate	Hz
q_j	power delivered by the j th NP	W
D	diameter of the heated area	m
H	fwhm of a Gaussian beam	m
S	side length of a square array	m
L	typical size of the heated area	m
P	interparticle distance	m
A	unit cell area of the NP lattice	m^2
N	total number of NPs	
r	radial coordinate	m
R	NP radius	m
d	NP diameter	m
V	NP volume	m^3
κ	thermal conductivity of the medium	$\text{W m}^{-1} \text{K}^{-1}$
κ_s	thermal conductivity of the substrate	$\text{W m}^{-1} \text{K}^{-1}$
ρ_{m}	mass density of the NP	kg m^{-3}
c_{m}	specific heat capacity of the NP	$\text{J K}^{-1} \text{kg}^{-1}$

amplitude experienced by the NP j . The heat power delivered q_j by each NP j is directly related to its absorption cross section σ_{abs} through the relation²⁹

$$q_j = \sigma_{\text{abs}} \frac{n\varepsilon_0 c}{2} |\mathbf{E}_j^{\text{ext}}|^2 \quad (1)$$

σ_{abs} can be estimated for spherical metal NPs using Mie theory.³⁰ The determination of the $\mathbf{E}_j^{\text{ext}}$ amplitudes is a self-consistent problem that can be solved using the discrete dipole approximation (DDA) method.^{28,29} When the NPs are far enough so that they can be considered as optically independent, the heat powers q_j delivered by the NPs will be identical and equal to

$$q = \sigma_{\text{abs}} I \quad (2)$$

where $I = [(n\varepsilon_0 c)/2]|\mathbf{E}_0|^2$ is the irradiance of the illumination (power per unit surface). This approximation is valid if the NP interdistance is at least 4 or 5 times larger than the NP diameter.^{32,33}

The temperature increase of a unique *spherical* NP of radius R releasing a heat power q and embedded in a homogeneous medium of thermal conductivity κ is simply given by

$$\Delta T = \frac{q}{4\pi\kappa R} \quad (3)$$

When this particle is located close to the interface between two homogeneous media of different thermal conductivities (κ and κ_s in our case), the NP temperature increase can be derived using the charge image method^{29,34} in analogy with electrostatics. When the NP is right at the interface, it simply yields

$$\Delta T = \frac{q}{4\pi\bar{\kappa}R} \quad (4)$$

where $\bar{\kappa} = (\kappa + \kappa_s)/2$ is the average conductivity. In the following, we will consider this situation where the NPs are located at the interface between two media, since it is the most common situation encountered experimentally.

However, when the NP is not spherical, no simple expression exists to estimate its temperature increase from the knowledge of the absorption cross section. To solve this problem, the common approach is to use eq 4 with a fictitious NP radius R_L instead of R :

$$\Delta T = \frac{q}{4\pi\bar{\kappa}R_L} \quad (5)$$

We have recently shown²⁹ that R_L , which we named the Laplace radius, can be retrieved by inverting a simple matrix \mathbf{A} defined as

$$A_{ij} = 1/|\mathbf{r}_i - \mathbf{r}_j|, \quad \text{for } i \neq j \quad (6)$$

$$A_{ij} = 2/a, \quad \text{for } i = j$$

where \mathbf{r}_j are the positions of the vertices of a regular three-dimensional meshing of the NP and a is the size of the unit cell of the meshing. The Laplace radius then simply reads

$$R_L = \sum_{i,j} (A^{-1})_{ij} \quad (7)$$

Note that for simple shapes such as rods, discs, ellipsoids, or tori, the fictitious radii to put in eq 4 for various aspect ratios have been calculated using another numerical approach (the boundary element method^{35,36}) and then fitted by analytical formulas in ref 4.

We consider now an *assembly* of N identical NPs. The temperature increase ΔT_j experienced by a given NP j stems from two contributions:

$$\Delta T_j = \Delta T_j^s + \Delta T_j^{\text{ext}} \quad (8)$$

ΔT_j^s is the self-contribution. It can be calculated using the above-mentioned eq 3, 4, or 5. The second contribution ΔT_j^{ext} is due to the heat delivered by the $N - 1$ other NPs located at \mathbf{r}_k surrounding the NP j under study. It reads

$$\Delta T_j^{\text{ext}} = \sum_{\substack{k=1 \\ k \neq j}}^N \frac{q_k}{4\pi\bar{\kappa}} \frac{1}{|\mathbf{r}_j - \mathbf{r}_k|} \quad (9)$$

Let us now define important notations: ΔT_0^{ext} stands for the external temperature experienced by the NP located *at the center* of the array (in this work, subscript "0" means "at the center"), ΔT_0^s stands for its self-temperature increase, and $\Delta T_0 = \Delta T_0^s + \Delta T_0^{\text{ext}}$ is its total temperature increase.

The temperature increase ΔT_0 observed at the center of an ensemble of plasmonic NPs was first discussed by Govorov *et al.* in 2006.²⁶ The authors explained that ΔT_0 cannot be estimated by considering the NPs individually. ΔT_0 is usually enhanced when the NPs are in close proximity due to the contribution of ΔT_0^{ext} . Useful formulas giving the order of magnitude of ΔT_0 were introduced, depending on the dimensionality of the system. In 2009, Richardson *et al.* evidenced that the temperature distribution created by gold NPs in solution can be strongly localized around each NP or, on the contrary, completely uniform throughout the solution, depending on the NP concentration and the laser intensity.²⁷

In the following, we will further investigate this problem by considering periodic (or pseudoperiodic) NP distributions (like the ones in Figure 1 for instance). In particular, we will show that eq 9, giving ΔT_0^{ext} , can be recast into simple analytical formulas. We will address the cases of one-dimensional (line) and two-dimensional NP lattices and different usual geometries (square and hexagonal).

1D Lattice. We consider in this section a linear chain of $N = 2\nu + 1$ metal NPs, spherical or not, with an interdistance p (Figure 2a) lying on a planar substrate under continuous (CW) illumination. In the following, R stands for the actual NP radius in the case of spherical NPs or for the Laplace radius R_L in the case of non-spherical NPs.

For such a system, one can derive a simple formula giving the collective temperature increase ΔT_0^{ext} at the center of the chain. If we assume that the NPs are not optically coupled (if $p > 4d$ typically^{32,33}), the heat generation q_j is identical in each NP and is given by eq 2. In this case, we can simply recast eq 9 into

$$\Delta T_0^{\text{ext}} = \frac{q}{4\pi\bar{\kappa}p} \sum_{\substack{j=-\nu \\ j \neq 0}}^{\nu} \frac{1}{j} \quad (10)$$

For N large enough, the estimation of the sum over j yields an approximation of the temperature increase of

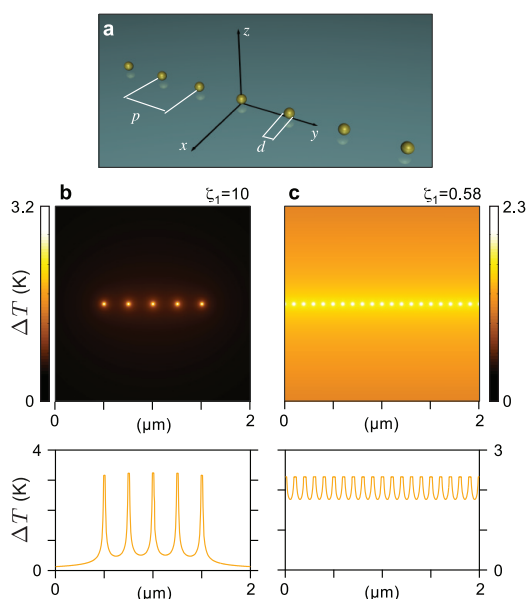


Figure 2. (a) Representation of a chain of N gold NPs lying on a glass substrate and immersed in water. (b) Calculated temperature distribution across a NP chain defined by $(N, p, d) = (5, 250 \text{ nm}, 15 \text{ nm})$, illuminated under $I = 1.27 \times 10^9 \text{ W m}^{-2}$, along with the associated temperature cross cut. This case corresponds to a temperature confinement regime. (c) Calculated temperature distribution across a NP chain defined by $(N, p, d) = (1001, 100 \text{ nm}, 25 \text{ nm})$, illuminated under $I = 1.27 \times 10^8 \text{ W m}^{-2}$, along with the associated temperature cross cut. This case corresponds to a temperature delocalization regime.

the cell located at the center of the chain:

$$\Delta T_0^{\text{ext}} \approx \frac{q}{2\pi k} \frac{\ln(\beta N)}{p} \quad (11)$$

while the self-contribution to the temperature increase of the NP located at the center of the lattice ΔT_0^{ext} is simply given by eq 4. In eq 11, $\beta = e^{\gamma}/2 \approx 0.890$ where $\gamma \approx 0.577$ is the Euler constant. The $\ln N/p$ dependence of ΔT_0^{ext} was derived by Govorov *et al.* in ref 26. Here we give the complete expression including the actual prefactor 1/2 and the first-order correction represented by β , which makes this expression accurate even for small numbers of NPs down to $N = 3$.

In order to estimate the relative contributions of ΔT_0^{ext} and ΔT_0^{ext} , we define the dimensionless number ζ_1 defined as the order of magnitude of the ratio between ΔT_0^{ext} and ΔT_0^{ext} . Subscript 1 refers to the one-dimensional nature of the array ($m = 1$). Using eq 4 and eq 11, one finds

$$\zeta_1 = \frac{p}{2R \ln N} \quad (12)$$

Note that the first-order correction factor β was omitted in the definition of ζ_1 , as the aim of the dimensionless parameters defined in this work is just to give orders of magnitude. ζ_1 gives thus an idea of which term is dominant in eq 8. Two regimes can be distinguished: (i) when ΔT_0^{ext} is dominant, *i.e.*, when $\zeta_1 \gg 1$, one can observe a regime where the NPs feature a temperature

increase that is unaffected by the other particles, as if they were isolated. In this case the temperature distribution is confined around each NP. (ii) When ΔT_0^{ext} is dominant, $\zeta_1 \ll 1$, it corresponds to a regime where the temperature distribution is extended and smooth all over the line. The temperature of each NP is mostly due to the overall heating of the $N - 1$ other neighboring particles.

Figure 2b,c present numerical simulations that illustrate these two regimes. The simulations were carried out using a Green's function formalism.²⁹ The NPs are lying on a glass substrate ($\kappa_s = 1.38 \text{ W m}^{-1} \text{ K}^{-1}$, $n_s = 1.5$) and immersed in water ($\kappa = 0.6 \text{ W m}^{-1} \text{ K}^{-1}$, $n = 1.33$). They are uniformly illuminated at $\lambda = 532 \text{ nm}$. The absorption cross sections σ_{abs} of the NPs (15 and 25 nm in diameter) were calculated using Mie theory, which gave 218 and 1054 nm², respectively. Figure 2b illustrates a regime where the temperature is highly localized around each NP. It corresponds to a confinement parameter $\zeta_1 = 10$. The confinement regime is obtained most of the time when working with one-dimensional distributions of NPs due to the slow logarithmic dependence of ΔT_0^{ext} with the number of particles N . To achieve a delocalization regime in 1D, as observed in Figure 2c, one needs to illuminate a very large amount of NPs in close proximity. Moreover, when illuminating a linear chain of NPs with a circular beam, most of the incident light does not illuminate the NPs, and a high laser power is usually required to achieve a temperature increase of a few degrees. For instance, in Figure 2b, $I = 1.27 \times 10^9 \text{ W m}^{-2}$ corresponds to a power of $P = 1 \text{ mW}$ focused on this 5-NP $1 \mu\text{m}$ long chain, while in Figure 2c, $I = 1.27 \times 10^8 \text{ W m}^{-2}$ corresponds to a power of $P = 1 \text{ W}$ illuminating the whole chain over a circular area of $100 \mu\text{m}$ in diameter.

2D Lattice. We shall now focus on the most common and useful case, which is the optical heating of *two-dimensional* (2D) lattices of metal NPs. Experimentally, several types of 2D lattices were reported in the literature (see Figure 1). Most of the time, the unit cell of the lattice is either hexagonal or square. In any case, we shall name the lattice parameter p (particle interdistance) and the area of the unit cell A . For a square unit cell,

$$A = p^2 \quad (13)$$

and for an hexagonal unit cell,

$$A = \sqrt{3}p^2/2 \quad (14)$$

Regarding the incoming beam, two cases will be considered: a Gaussian beam or a circular, uniform beam. In the case of a uniform, circular illumination of diameter D , the irradiance reads

$$I = \frac{4P}{\pi D^2} \quad (15)$$

where P is the power of the laser. In the case of a Gaussian beam, the irradiance at the sample location in

radial coordinates reads

$$I(r) = \frac{P}{2\pi\sigma^2} e^{-r^2/2\sigma^2} \quad (16)$$

We define $H = 2(2 \ln 2)^{1/2}\sigma$ as the fwhm of the beam. Under Gaussian illumination, the irradiance I to be used to calculate ΔT_0^s is the one at the center of the array $I(0) = P/2\pi\sigma^2$. This yields this expression of ΔT_0^s :

$$\Delta T_0^s = \frac{\sigma_{\text{abs}} I(0)}{4\pi\bar{\kappa}R} = \frac{\ln 2 \sigma_{\text{abs}} P}{\pi^2 H^2 \bar{\kappa} R} \quad (17)$$

Regarding the collective temperature increase ΔT_0^{ext} , it can be calculated from eq 9, just like in the 1D case by calculating the limit when the number of particles is large. In the 2D case, the expression depends on the nature of the array (infinite or square) and the illumination conditions (Gaussian or circular uniform). The estimations of ΔT_0^{ext} in these different situations are summarized in Table 2.

TABLE 2. Expression Giving an Estimation of the Collective Temperature Increase ΔT_0^{ext} for Typical Array Geometries and Various Illumination Conditions

Case 1: Gaussian illumination of an infinite array

$$\Delta T_0^{\text{ext}} \approx \frac{\sigma_{\text{abs}} P}{\bar{\kappa}} \sqrt{\frac{\ln 2}{4\pi}} \frac{1}{HA} \left(1 - \frac{4\sqrt{\ln(2A)}}{\pi H} \right) \quad (18)$$

Case 2: Uniform and circular illumination of an infinite array

$$\begin{aligned} \Delta T_0^{\text{ext}} &\approx \frac{\sigma_{\text{abs}} P}{\bar{\kappa}} \frac{1}{\pi DA} \left(1 - \frac{2\sqrt{A}}{\sqrt{\pi D}} \right) \\ \Delta T_0^{\text{ext}} &\approx \frac{\sigma_{\text{abs}} I}{\bar{\kappa}} \frac{1}{4A} \left(1 - \frac{2\sqrt{A}}{\sqrt{\pi D}} \right) \end{aligned} \quad (19)$$

Case 3: Uniform illumination of a finite-size square array

$$\Delta T_0^{\text{ext}} \approx \frac{\sigma_{\text{abs}} I}{\bar{\kappa}} \frac{\ln(1 + \sqrt{2})}{\pi} \frac{S}{p^2} \quad (20)$$

In the second case of Table 2, two equivalent expressions are provided, depending on whether the power P or the irradiance I of the incoming light is considered. All these equations feature a first-order correction in p/L that makes them accurate even for a small number of NPs, down to $N \approx 9$. The derivation of all these formulas is provided in the Supporting Information. Note that all these formulas follow Govorov's general trend introduced in ref 26, which reads

$$\Delta T_0 \propto \Delta T_0^s \frac{RN^{(m-1)/m}}{p} \text{ for } m \geq 2 \quad (21)$$

where N is the total number of NPs, R their radius, and m the dimensionality of the system ($m = 2$ in the current case).

Just like the previous 1D case, two regimes can be distinguished when illuminating a 2D distribution of NPs: a confinement regime, where the temperature increase is localized around each NP, and a delocalization regime, where an extended and smooth temperature

distribution is observed throughout the whole array despite the nanometric size of the particles. The occurrence of one regime or another can be predicted by considering a dimensionless parameter ζ_2 that estimates the ratio $\Delta T_0^s/\Delta T_0^{\text{ext}}$. For any 2D distribution

$$\zeta_2 = \frac{p^2}{3LR} \quad (22)$$

where L stands for the characteristic size of the illuminated area. For instance, L is the beam diameter D in the case of a circular uniform beam, it is H for a Gaussian illumination, or it is the size S of an illuminated square array. The subscript of ζ_2 refers to the two-dimensional nature of the NP distribution.

Figure 3 illustrates these results with numerical simulations of 2D temperature distributions carried out using a Green's function formalism.²⁹ The illumination wavelength was set to $\lambda = 532$ nm. The absorption cross sections of the NPs were calculated using Mie theory ($\sigma_{\text{abs}} = 218$ nm² for $R = 7.5$ nm and $\sigma_{\text{abs}} = 4434$ nm² for $R = 20$ nm). All the cases reported in Table 2 have been considered: case 1 with a hexagonal lattice (Figure 3d), case 1 with a square lattice (Figure 3e), case 2 with a hexagonal lattice (Figure 3f), case 2 with a square lattice (Figure 3g), and case 3 (Figure 3h). The confinement parameters span from 0.06 to 3.3. One can see that a collective effect occurs most of the time, unless there is a very low number of NPs, like in Figure 3h. In each of the five situations, ΔT_0^s and ΔT_0^{ext} have been calculated using eq 4 and eq 18, 19, or 20, respectively, and their values have been reported on the temperature cross cut below each image. A very good agreement is observed between these values obtained using simple formulas and the exact Green's function simulations in two dimensions. This agreement illustrates the ability of the simple formulas reported in Table 2 to estimate ΔT_0^s and ΔT_0^{ext} , which are the two important features when heating a NP array.

Experimental Illustration. We recently developed an optical microscopy technique able to quantitatively map the temperature distribution around nanometric sources of heat.³¹ This microscopy technique, named TIQSI for thermal imaging using quadriwave shearing interferometry, is based on the thermal-induced variation of the refractive index of the medium surrounding the nanosources of heat. In this section, we report on experimental results using the TIQSI technique carried out to support the above-mentioned theoretical framework. The purpose of this section is twofold: First, we aim at experimentally evidencing the two regimes. Second, we wish to validate eq 18, 19, or 20.

Results presented in Figure 4 are aimed at evidencing the two regimes. The samples consist of lithographic gold nanodiscs or nanodots distributed according to a finite-size regular square lattice (Figure 4a,b). Three measurements are presented corresponding to various

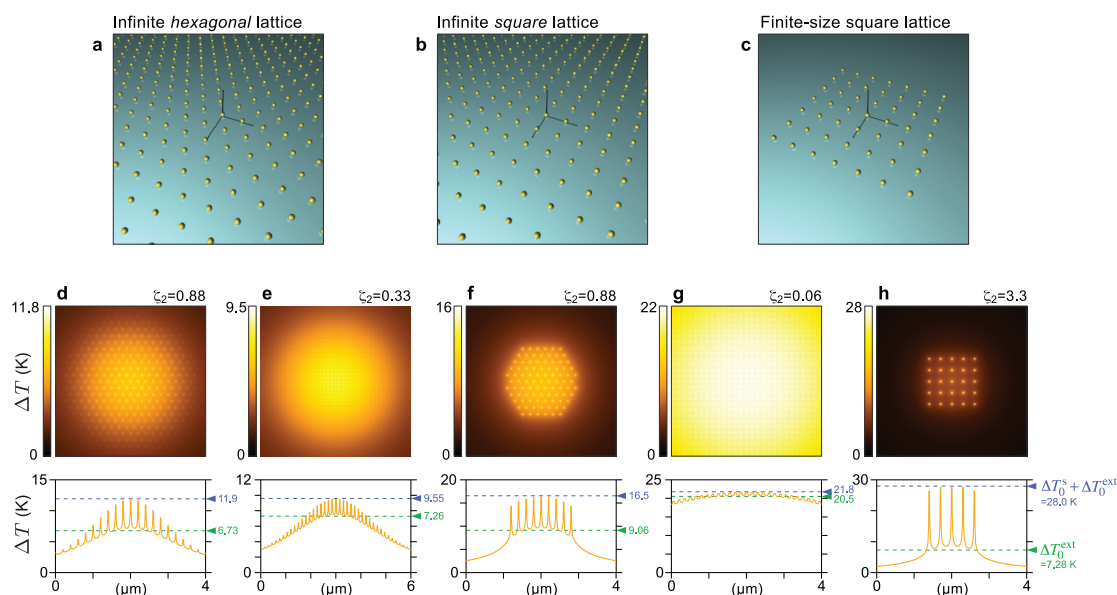


Figure 3. (a, b, c) Three-dimensional representations of the three kinds of regular lattices of gold nanospheres used in the simulations. The nanospheres are deposited on a glass substrate and immersed in water. (d) Temperature distribution throughout a periodic and infinite hexagonal lattice of NPs illuminated by a Gaussian beam ($p = 200$ nm, $d = 15$ nm, $H = 2$ μ m, $P = 10$ mW). (e) Temperature distribution throughout an infinite and periodic square lattice of NPs illuminated by a Gaussian beam ($p = 150$ nm, $d = 15$ nm, $H = 3$ μ m, $P = 10$ mW). (f) Temperature distribution throughout an infinite and periodic hexagonal lattice of NPs illuminated by a uniform circular beam ($p = 200$ nm, $d = 15$ nm, $D = 2$ μ m, $P = 10$ mW). (g) Temperature distribution throughout an infinite and periodic square lattice of NPs illuminated by a uniform circular beam ($p = 150$ nm, $d = 40$ nm, $D = 6$ μ m, $P = 2$ mW). (h) Temperature distribution throughout a finite-size square lattice of NPs, uniformly illuminated ($p = 300$ nm, $d = 15$ nm, $N = 5 \times 5$, $I = 5.7 \times 10^9$ W m $^{-2}$). In each case, the collective contribution to the temperature increase ΔT_0^{ext} calculated at the center of the lattice using eq 18, 19, or 20 is indicated. The self-contribution to the temperature ΔT_0^{ext} calculated using eq 4 is also represented.

values of the confinement parameter ζ_2 (Figure 4c,e,g), namely, 1.66, 0.37, and 0.18. In each case, a numerical simulation of the temperature distribution supports the experimental measurements (Figure 4d,f,h). These results highlight the fact that a high degree of temperature confinement at the vicinity of the NPs requires a small number of NPs and a large interdistance. They also illustrate the ability of ζ_2 to properly estimate the degree of temperature confinement.

Results presented in Figure 5 are aimed at comparing the temperature increase predicted using eq 18, 19, or 20 with temperatures observed experimentally. We chose to use a sample consisting of a quasi-periodic array of spherical gold NPs. The sample was made by diblock copolymer lithography.²⁰ The advantage of this approach compared to lithographic samples is to provide a distribution of *spherical* NPs, which permits a much easier estimation of the expected NP absorption cross section using Mie theory. Furthermore, the NP distribution is uniform and covers the whole 1 inch sample. Experimentally, the sample was illuminated by a uniform circular beam of diameter $D = 24.3$ μ m at $\lambda = 532$ nm. The NPs were lying on a glass substrate ($\kappa_s = 1.38$ W m $^{-1}$ K $^{-1}$) and immersed in water ($\kappa = 0.6$ W m $^{-1}$ K $^{-1}$). Figure 5a presents the temperature map measured for a laser power of $P = 17.9$ mW. A central temperature increase of $\Delta T_0 = 25.0$ K is measured.

We shall now see to what extent this actual temperature increase can be predicted by the above

derived theory, using eq 19. In order to use such a formula, one has to know the geometric features of the lattice, along with the absorption cross section of a NP, the beam diameter, and the laser power. SEM images of the investigated sample led to a NP average radius $\bar{R} = 11.43 \pm 0.56$ nm (Figure 5c) and an average interdistance $\bar{p} = 86.4 \pm 2.2$ nm. The diameter of the illuminated area was $D = 24.3 \pm 0.8$ μ m. The laser power was $P = 17.9 \pm 0.5$ mW. The absorption cross section of a NP can be retrieved from the knowledge of its radius. Since the radius distribution is slightly broad, we did not consider the absorption cross section calculated from the mean radius value: $\bar{\sigma}_{\text{abs}} = \sigma_{\text{abs}}^{\text{Mie}}(\bar{R})$. Instead, we computed the cross sections of all the NPs of a given SEM image (see the histogram in Figure 5c) and took the average:

$$\bar{\sigma}_{\text{abs}} = \frac{1}{N} \sum_{j=1}^N \sigma_{\text{abs}}^{\text{Mie}}(R_j) \quad (23)$$

where R_j is the radius of the j th NP. This caution leads in principle to a much more faithful estimation of the actual mean absorption cross section. Indeed, for small radii, the absorption cross section scales as R^3 . When a function f is not linear, the average $\langle f(x) \rangle$ is not equivalent to $f(\langle x \rangle)$.

We found a NP mean absorption cross section equal to $\bar{\sigma}_{\text{abs}} = 810 \pm 115$ nm 2 . This uncertainty comes from the dispersion of the NP radius distribution measured

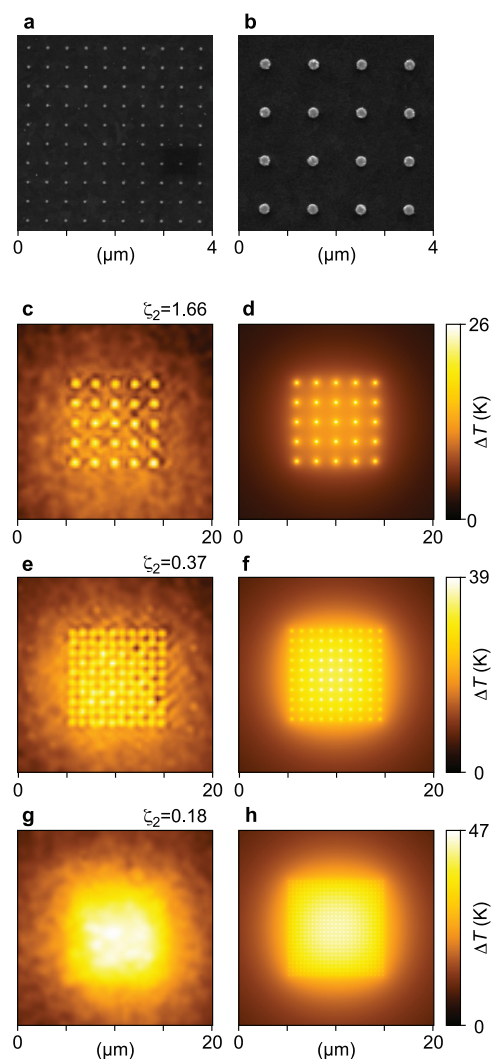


Figure 4. (a) SEM image of a regular pattern of gold nanodots made by e-beam lithography ($p = 400$ nm, $d = 60$ nm). (b) SEM image of a regular pattern of gold nanodiscs made by e-beam lithography ($d = 200$ nm, $p = 1$ μ m). (c) Experimental temperature distribution measured on a pattern of 5×5 gold nanodiscs corresponding to a confinement parameter $\zeta_2 = 1.66$ ($p = 2$ μ m, $d = 200$ nm). (d) Associated numerical simulation of the temperature. (e) Experimental temperature distribution measured on a pattern of 10×10 gold nanodiscs, $\zeta_2 = 0.37$ ($p = 1$ μ m, $d = 200$ nm). (f) Associated numerical simulation. (g) Experimental temperature distribution measured on a pattern of gold nanodots, $\zeta_2 = 0.18$ ($p = 400$ nm, $d = 60$ nm, $S = 10$ μ m). (h) Associated numerical simulation.

on the SEM images (see Figure 5c). As the absorption cross section varies as R^3 for small NPs, the relative error on σ_{abs} is around three times larger than the relative error on R . Figure 5b displays the extinction spectra measured on the investigated sample. The fact that the resonance appears at $\lambda = 520$ nm on glass in air is evidence that the NPs are spherical and that there is no optical interparticle coupling. Hence, Mie theory can be wisely used to estimate the absorption cross section. From this series of parameters, eq 19 gives an expected temperature increase of $\Delta T = 29.8 \pm 4.5$ $^{\circ}$ C. This theoretical value is consistent with the measured

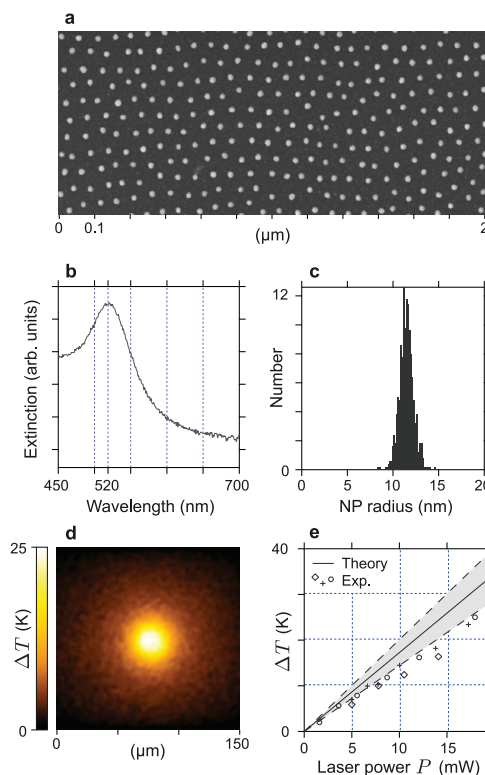


Figure 5. (a) SEM image of a quasi-hexagonal array of gold NPs obtained by diblock copolymer lithography. (b) Extinction spectra of the sample in air featuring a plasmonic resonance at 520 nm. (c) Histogram of the NP radius distribution (determined automatically using ImageJ). (d) Temperature image measured using the TIQSI technique when illuminating the gold NP array with a beam radius of 24 μ m. (e) Expected temperature increase as a function of the laser power using eq 19 (solid line, the gray area corresponds to the error), and experimental measurements of the temperature increase using the TIQSI technique at various laser powers and at three different locations on the sample (crosses, circles, and diamonds).

temperature increase $\Delta T = 25.0$ $^{\circ}$ C. The small bias could come from the difficulty to precisely estimate the actual irradiance experienced by the NPs or their actual mean absorption cross section using Mie theory. This result illustrates the fact that the derived expressions 18, 19, and 20 give a good estimation of the order of magnitude of the temperature over an illuminating pattern of absorbing NPs.

To close this section, we wish to illustrate the method on a practical case taken from the literature. In 2009, Righini *et al.* reported on the optical trapping of *Escherichia coli* bacteria, assisted by plasmonic gold dimer nanoantennas.³⁷ The experiment consisted basically in illuminating a periodic array of gold nanoantennas made of two rods, 500 nm long each, separated by a 30 nm gap. While the purpose of this illumination was to trap bacteria, the question was raised whether a temperature increase could occur in the system due to light absorption by the antennas. This is typically the experimental situation where our approach can apply and provide missing information. The parameters of

the system were the following: $D = 100 \mu\text{m}$, $p = 10 \mu\text{m}$, square lattice, $d_x = 1 \mu\text{m}$, $d_y = 110 \text{ nm}$, $\kappa = 0.6 \text{ W m}^{-1} \text{ K}^{-1}$ (water), $\kappa_s = 1.38 \text{ W m}^{-1} \text{ K}^{-1}$ (glass substrate), $\bar{\kappa} = 0.99 \text{ W m}^{-1} \text{ K}^{-1}$, $P = 300 \text{ mW}$.

Let us first estimate the degree of temperature confinement expected in this experiment. For this purpose, the parameter ζ_2 given by eq 22 has to be calculated, and it yields, $\zeta_2 \approx 1$. Hence, the collective effects in these experimental conditions cannot be neglected and ΔT_0^{ext} is on the same order of magnitude as the temperature increase ΔT_0^{f} generated by a single gold structure.

Let us now calculate the self-contribution to the temperature increase at the center of the array ΔT_0^{f} using eq 5. For this purpose, the Laplace radius R_L and the absorption cross section σ_{abs} have to be determined. Equation 7 gives $R_L = 207 \text{ nm}$, and the absorption cross section is on the order of $3 \times 10^5 \text{ nm}^2$ (calculated using the boundary element method^{35,36}). Equation 5 thus gives $\Delta T_0^{\text{f}} \approx 4.4 \text{ K}$.

Let us finally compute the collective temperature increase ΔT_0^{ext} . Equation 19 has to be used since the array is uniformly illuminated over a circular area, and the unit cell area A equals p^2 since the unit cell is a square. We end up with $\Delta T_0^{\text{ext}} \approx 2.6 \text{ K}$.

As a conclusion, the self- and collective temperature increases are on the same order of magnitude, as predicted by the calculation of ζ_2 . More precisely, an overall temperature increase around $\Delta T_0^{\text{ext}} \approx 2.6 \text{ K}$ is expected around the center of the lattice, along with a local additional temperature increase of $\Delta T_0^{\text{f}} \approx 4.4 \text{ K}$ at the vicinity of each nanostructure. Hence, a bacterium should experience a temperature increase of around 7 K when trapped and 2.6 K when untrapped. Such a small temperature increase rules out *a priori* any possible damage to the bacterium or any thermal-induced fluid convection¹⁷ that would affect the trapping forces. This was a practical case showing the valuable information that can be provided by our theoretical framework.

Pulsed Illumination. In this last section, we discuss the influence of a pulsed illumination on the temperature spatial confinement throughout a NP array. We consider a pulsed illumination with a pulsation rate f , a pulse duration τ_p (typically smaller than a picosecond), and a time-averaged irradiance $\langle I \rangle$.

Using nano- to femtosecond pulsed illumination modifies drastically the dynamics of the temperature profile around an absorbing NP. In particular, the temperature increase at the vicinity of a NP can reach extreme values just after a pulse absorption. The inner temperature impulse of a NP following a single pulse absorption can be estimated using the expression³⁰

$$\Delta T^{\text{fs}} = \frac{\sigma_{\text{abs}} \langle I \rangle}{fV\rho_m c_m} \quad (24)$$

where V is the volume of the NP, ρ_m the NP mass density, and c_m its specific heat capacity. This brief and intense temperature increase is already used in some applications, *e.g.*, in photoacoustic imaging where the brief and intense temperature increase that occurs at the vicinity of the NP generates a shockwave.³⁸ Hence, the meaningful quantity to consider under pulsed illumination is not the average temperature over time, but rather the maximum temperature achieved at each location of the sample during the evolution:

$$T_{\text{max}}(r) = \max_t(T(r, t)) \quad (25)$$

$T_{\text{max}}(r)$ is what we name the *temperature envelope*. Under femtosecond-pulsed illumination, $T_{\text{max}}(r)$ features a confined $1/|r|^3$ profile,³⁰ unlike the steady-state temperature distribution under CW illumination, which features a $1/|r|$ profile. The derivation of these dependences is provided in the Supporting Information.

Another physical quantity under pulsed illumination that is worth discussing is the time-average temperature profile $\bar{T}(r)$, which can be defined as

$$\bar{T}(r) = \langle T(r, t) \rangle_t = f \int_0^{1/f} T(r, t) dt \quad (26)$$

Unlike the temperature envelope $T_{\text{max}}(r)$, the average temperature $\bar{T}(r)$ under pulsed illumination of a single NP always spreads out according to a $1/|r|$ law (see the Supporting Information), just like in CW illumination, which is much broader than the $1/|r|^3$ spatial extension of the temperature envelope. Hence, it is important to note that the enhanced spatial confinement of the temperature usually put forward under pulsed illumination concerns only the *temperature envelope* and not the mean temperature.

Let us consider now an array of NPs. In typical experimental conditions, using femtosecond-pulsed illumination usually leads to a confinement regime due to the $1/|r|^3$ profile and to the fact that the series $\sum 1/j^3$ is not divergent (unlike $\sum 1/j$). However, a spatial confinement is not systematic. Indeed, a temperature confinement may not occur in two situations: (i) when the thermal inertia of a NP is such that the NP has no time to cool between two successive pulses; this effect usually occurs when the NP size is too large; (ii) when the number of NPs in the array is such that the NP temperature impulse following the pulse absorption is insignificant compared to the collective temperature increase ΔT_0^{ext} throughout the array. Hence, in order to expect a temperature confinement under pulsed illumination, two conditions have to be fulfilled. Just like in the previous sections, we will characterize these conditions with dimensionless numbers that have to be compared with unity. Let us now further investigate these two conditions.

The first condition to fulfill in order to achieve a temperature confinement under pulsed illumination is to have a NP thermal relaxation time faster than the

time-lapse $1/f$ between two successive pulses. We derived the relaxation time of a single NP under pulse illumination in a previous article.³⁰ It reads

$$\tau_d^{\text{NP}} = R^2 \frac{\rho_m c_m}{3\bar{\kappa}} \quad (27)$$

The first confinement parameter in pulsed illumination, defined as $\eta^s = (f\tau_d^{\text{NP}})^{-1}$, thus reads

$$\eta^s = \frac{3\bar{\kappa}}{\rho_m c_m} \frac{1}{R^2 f} \quad (28)$$

The condition $\eta^s \gg 1$ ensures that the NP has enough time to cool between two successive pulses, which is a requirement to achieve the temperature confinement regime.

Interestingly, this confinement parameter η^s also equals $\Delta T^{\text{fs}}/\Delta T_0^s$ (see eq 3 and eq 24). Hence, η^s can also be understood as the order of magnitude of the ratio between the maximum temperature increase under single-pulse illumination and the temperature increase under CW illumination of a single NP.

The second condition to fulfill in order to achieve a temperature confinement under pulsed illumination is to achieve a temperature impulse ΔT^{fs} stronger than the collective temperature increase of the NP array ΔT_0^{ext} . The dimensionless parameter to consider is thus defined as the order of magnitude of $\Delta T^{\text{fs}}/\Delta T_0^{\text{ext}}$. For a 1D array, using eq 11 and eq 24, we can define this dimensionless parameter as

$$\eta_1^{\text{ext}} = \frac{3\bar{\kappa}}{2\rho_m c_m} \frac{p}{f R^3 \ln N} \quad (29)$$

and for a 2D array, using indifferently eq 18, 19, or 20 and eq 24, we find

$$\eta_2^{\text{ext}} = \frac{\bar{\kappa}}{\rho_m c_m} \frac{p^2}{f R^3 L} \quad (30)$$

In order to reach a confinement regime, the two conditions to be fulfilled are thus $\eta^s \gg 1$ and $\eta_m^{\text{ext}} \gg 1$, where m is the dimensionality of the system ($m = 1$ or 2). This amounts to saying that the instantaneous temperature impulse after a pulse absorption by a NP has to be larger than both ΔT_0^s and ΔT_0^{ext} . Interestingly, the three dimensionless numbers defined in this work are linked through the relation

$$\eta_m^{\text{ext}} = \eta^s \zeta_m \quad (31)$$

In practice, situations where a confinement regime is not observed despite the femtosecond-pulsed illumination occur typically while illuminating NP arrays over *macroscopic* areas (L large) or when illuminating arrays of *large* lithographic microstructures (R_L large).

For longer pulse durations (from picosecond to nanosecond), the initial temperature increase cannot be considered as instantaneous. Hence eq 24 does not apply, and the occurrence of the confinement regime cannot be determined using simple dimensionless

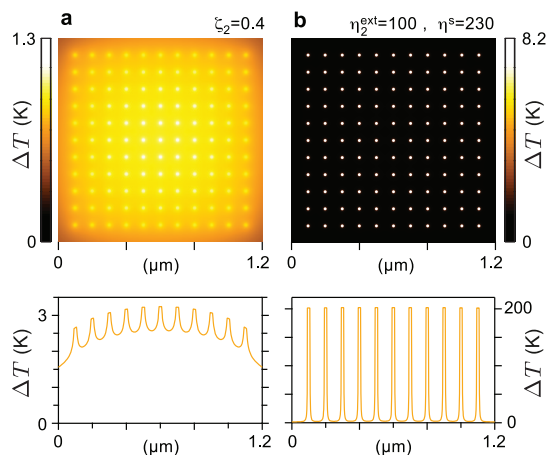


Figure 6. Numerical simulations carried out on a square ($1 \times 1 \mu\text{m}^2$) lattice of 16 nm spherical gold NPs with a particle interdistance of $p = 100$ nm. (a) Temperature map when illuminating the NP lattice with a CW uniform laser beam. $I = 3.2 \times 10^8 \text{ W m}^{-2}$. (b) Map of the temperature envelope when illuminating the NP lattice with a femtosecond-pulsed uniform laser beam at a pulsation rate of 80 MHz, featuring a much higher temperature confinement. $\langle I \rangle = 3.2 \times 10^8 \text{ W m}^{-2}$. The calculated parameters ζ_2 and η_2^{ext} and η^s characterizing the degree of temperature confinement (see eq 22, eq 28, and eq 30) are indicated on top of images a and b.

numbers. Numerical simulations are required in this case. Let us note that illustrating these theoretical results experimentally is for the time being out of reach since most of the temperature mapping techniques, including the TQSI technique, would not be sensitive to the temperature envelope $T_{\text{max}}(\mathbf{r})$, but to the time-average temperature $\bar{T}(\mathbf{r})$, which does not feature any confinement, as explained above.

Figure 6 illustrates this section. We consider a square array, $1 \mu\text{m} \times 1 \mu\text{m}$, composed of 16 nm NPs ($\sigma_{\text{abs}} = 265 \text{ nm}^2$) with an interdistance of $p = 100$ nm. Under CW illumination, this geometry yields $\zeta_2 \approx 0.33$, which corresponds to a delocalized temperature distribution, fairly uniform throughout the array, where the collective effect is dominant. The actual temperature distribution plotted in Figure 6a shows indeed a substantial contribution of a collective effect. The identical array under femtosecond-pulsed illumination at $f = 80$ MHz is associated with confinement parameters that equal $\eta^s \approx 230 \gg 1$ and $\eta_2^{\text{ext}} \approx 100 \gg 1$. Hence, the temperature envelope is expected to be much more confined around each NP. The actual temperature distribution, plotted in Figure 6b, features indeed a highly contrasted temperature distribution. This example illustrates how a femtosecond-pulsed illumination can efficiently contribute to confine a temperature distribution at close vicinity to NPs, while this cannot be achieved under CW illumination.

CONCLUSION

To summarize, this work is intended to help characterize theoretically the temperature distribution

when illuminating assemblies of nanoparticles, without carrying out simulations. For this purpose, we first derived simple formulas to estimate the expected temperature increase within an array of NPs under illumination for different lattice geometries (linear, square, hexagonal, finite, infinite) and illumination conditions (uniform, Gaussian). Then, depending on the geometry, we evidenced two distinct regimes: a temperature confinement regime, where a temperature increase is visible only in the vicinity of each NP, and a temperature delocalization regime, where the temperature is smooth all over the NP distribution despite the nanometric size of the NPs. In order to simply predict the occurrence of the temperature confinement regime, we derive dimensionless parameters ζ , η^s , and η^{ext} , which depend on the geometry

of the NP array, and the thermal physical constants of the system. Under CW illumination, a temperature spatial confinement is expected if $\zeta \gg 1$, and under femtosecond-pulsed illumination, a further enhanced temperature confinement is expected if the two conditions $\eta^s \gg 1$ and $\eta^{\text{ext}} \gg 1$ are fulfilled. Under pulsed illumination, we highlight the fact that the physical quantity that features enhanced spatial confinement is not the time-average temperature profile $\bar{T}(\mathbf{r})$, but the maximum temperature over time $T_{\text{max}}(\mathbf{r})$. Most of the numerical results are illustrated with experimental measurements performed on assemblies of gold nanoparticles using quadriwave lateral shearing interferometry. As a practical illustration, we have shown how our framework can apply in a recent reported experiment using NP arrays to trap bacteria.

METHODS

Fabrication of Extended Gold NP Arrays. The samples used in the experiments reported in Figure 5 were fabricated by diblock copolymer lithography. Here is the detailed procedure. In a typical synthesis, polystyrene(1056)-block-poly(2-vinylpyridine)-(495) (PS₁₀₅₆-b-P2VP₄₉₅) from Polymer Source Inc. was dissolved at room temperature in anhydrous toluene (Sigma-Aldrich) at a concentration of 5 mg/mL and stirred for 24 h. The quantity of gold precursor was calculated relative to the number of P2VP units (N_{P2VP}) with a loading parameter (L) equal to 0.5, that is, 1 molecule of HAuCl₄ for 2 P2VP monomers. Hydrogen tetrachloroaurate(III) trihydrate (HAuCl₄·3H₂O, Sigma-Aldrich) was added to the polymer solution, and the mixture was stirred for 24 h in a sealed glass vessel. Glass coverslips (Carl Roth) were cleaned in a piranha solution for at least 5 h and were extensively rinsed with Milli-Q water and dried under a stream of nitrogen. Gold-loaded micellar monolayers were prepared by dip-coating a glass coverslip into the previously prepared solutions with a constant velocity equal to 24 mm min⁻¹. To remove the organic template and form inorganic nanoparticles, the dip-coated glass slides were exposed to oxygen plasma (150 W, 0.15 mbar, 45 min, PVA TEPLA 100 Plasma System). The immobilized gold nanoparticles were enlarged by incubating the substrate for 20 min in 10 mL of an aqueous solution containing ethanolamine (2 mM) and KAuCl₄ (0.1 wt %) and then calcined at 450 °C for 1 h under nitrogen. Scanning electron measurements were performed with a Dual Beam (FIB/SEM) instrument (Quanta 3D FEG, FEI, Hillsboro).

Thermal Measurements Using TIQSI. Temperature measurements were performed by wavefront sensing using quadriwave shearing interferometry (QSI).³¹ Briefly, using this technique, a plane optical wavefront crosses the region of interest and undergoes a distortion due to the thermal-induced variation of the refractive index of the medium. This wavefront distortion is imaged quantitatively using a QSI wavefront analyzer. The source was a collimated light-emitting diode from Thorlabs whose emitting spectrum spans from 600 to 650 nm (ref: M625L2-C1). The QSI wavefront analyzer was purchased from Phisics SA (ref: Sid4Bio). Each image presented in this work is the result of the average of 30 wavefront images, corresponding to a whole acquisition time of around 3 s.

Conflict of Interest: The authors declare no competing financial interest.

Supporting Information Available: Derivations of the expressions of the collective temperature increase. Derivation of the temperature profiles under pulsed illumination. This material is available free of charge via the Internet at <http://pubs.acs.org>.

Acknowledgment. The authors acknowledge financial support from research French agency ANR grant Tkinet (ANR 2011 BSV5 019 05). This work was also partially supported by the European Community's Seventh Framework Program under grant ERC-Plasmolight (259196), and Fundació privada CELLEX. EBU acknowledges the support of the FPI fellowship from the Spanish Ministry of Science and Innovation (MICINN).

REFERENCES AND NOTES

- Biagioni, P.; Huang, J. S.; Hecht, B. Nanoantennas for Visible and Infrared Radiation. *Rep. Prog. Phys.* **2012**, *75*, 024402.
- Baffou, G.; Quidant, R. Thermo-Plasmonics: Using Metallic Nanostructures as Nano-Sources of Heat. *Laser Photonics Rev.* **2013**, *7*, 171–187.
- Qin, Z.; Bischof, J. C. Thermophysical and Biological Responses of Gold Nanoparticle Laser Heating. *Chem. Soc. Rev.* **2012**, *41*, 1191–1217.
- Baffou, G.; Quidant, R.; García de Abajo, F. J. Nanoscale Control of Optical Heating in Complex Plasmonic Systems. *ACS Nano* **2010**, *4*, 709.
- Lal, S.; Clare, S. E.; Halas, N. J. Nanoshell-Enabled Photothermal Cancer Therapy: Impending Clinical Impact. *Acc. Chem. Res.* **2008**, *41*, 1842.
- Cherukuri, P.; Glazer, E. S.; Curley, S. A. Targeted Hyperthermia Using Metal Nanoparticles. *Adv. Drug Delivery Rev.* **2010**, *62*, 339–345.
- Huang, X.; Jain, P. K.; El-Sayed, I. H.; El-Sayed, M. A. Plasmonic Photothermal Therapy (PPTT) Using Gold Nanoparticles. *Laser Med. Sci.* **2008**, *23*, 217–228.
- Urban, A.; Pfeiffer, T.; Fedoruk, M.; Lutich, A.; Feldmann, J. Single Step Injection of Gold Nanoparticles through Phospholipid Membranes. *ACS Nano* **2011**, *5*, 3585–3590.
- Han, G.; Ghosh, P.; De, M.; Rotello, V. M. Drug and Gene Delivery Using Gold Nanoparticles. *NanoBioTechnology* **2007**, *3*, 40.
- Ghosh, P.; Han, G.; De, M.; Kim, C. K.; Rotello, V. M. Gold Nanoparticles in Delivery Applications. *Adv. Drug Delivery Rev.* **2008**, *60*, 1307–1315.
- Timko, B. T.; Dvir, T.; Kohane, D. S. Remotely Triggerable Drug Delivery Systems. *Adv. Mater.* **2010**, *22*, 4925.
- Cognet, L.; Berciaud, S.; Lasne, D.; Lounis, B. Photothermal Methods for Single Nonluminescent Nano-Objects. *Anal. Chem.* **2008**, *80*, 2288–2294.
- Copland, J.; Eghtedari, M.; Popov, V. L.; Kotov, N.; Mamedova, N.; Motamedi, M.; Oraevsky, A. Bioconjugated Gold Nanoparticles as a Molecular Based Contrast Agent: Implications

- for Imaging of Deep Tumors Using Optoacoustic Tomography. *Mol. Imaging Biol.* **2004**, *6*, 341–349.
14. Challener, W. A.; Peng, C.; Itagi, A. V.; Karns, D.; Peng, W.; Peng, Y.; Yang, X. M.; Zhu, X.; Gokemeijer, N. J.; Hsia, Y.-T.; *et al.* Heat-Assisted Magnetic Recording by a Near-Field Transducer with Efficient Optical Energy Transfer. *Nat. Photonics* **2009**, *3*, 220.
 15. Nitzan, A.; Brus, L. E. Theoretical Model for Enhanced Photochemistry on Rough Surfaces. *J. Chem. Phys.* **1981**, *75*, 2205.
 16. Cao, L.; Barsic, D.; Guichard, A.; Brongersma, M. Plasmon-Assisted Local Temperature Control to Pattern Individual Semiconductor Nanowires and Carbon Nanotubes. *Nano Lett.* **2007**, *7*, 3523–3527.
 17. Donner, J.; Baffou, G.; McCloskey, D.; Quidant, R. Plasmon-Assisted Optofluidics. *ACS Nano* **2011**, *5*, 5457–5462.
 18. Acimovic, S.; Kreuzer, M. P.; González, M. U.; Quidant, R. Plasmon Near-Field Coupling in Metal Dimers as a Step Toward Single-Molecule Sensing. *ACS Nano* **2009**, *3*, 1231–1237.
 19. Anker, J. N.; Hall, P. W.; Lyandres, O.; Shah, N. C.; Zhao, J.; Van Duyne, P. Biosensing with Plasmonic Nanosensors. *Nat. Mater.* **2008**, *7*, 442–453.
 20. Zhu, M.; Baffou, G.; Meyerbröcker, N.; Polleux, J. Micropatterning Thermoplasmonics Gold Nanoarrays to Manipulate Cell Adhesion. *ACS Nano* **2012**, *6*, 7227–7233.
 21. Corrigan, T. D.; Guo, S.; Phaneuf, R. J.; Szacinski, H. Enhanced Fluorescence from Periodic Arrays of Silver Nanoparticles. *J. Fluoresc.* **2005**, *15*, 777–784.
 22. Moran, A. M.; Sung, J.; Hicks, E. M.; Van Duyne, P.; Spears, K. G. Second Harmonic Excitation Spectroscopy of Silver Nanoparticle Arrays. *J. Phys. Chem. B* **2005**, *109*, 4501–4506.
 23. Féridj, N.; Aubard, J.; Lévi, G.; Krenn, J. R.; Hohenau, A.; Schider, G.; Leitner, A.; Aussenegg, F. R. Optimized Surface-Enhanced Raman Scattering on Gold Nanoparticle Arrays. *Appl. Phys. Lett.* **2003**, *82*, 3095.
 24. Le, F.; Brandl, D. W.; Urzhumov, Y. A.; Wang, H.; Kundu, J.; Halas, N. J.; Aizpurua, J.; Nordlander, P. Metallic Nanoparticle Arrays: A Common Substrate for Both Surface-Enhanced Raman Scattering and Surface-Enhanced Infrared Absorption. *ACS Nano* **2008**, *2*, 707–718.
 25. Baudrion, A. L.; Perron, A.; Veltri, A.; Bouhelier, A.; Adam, P. M.; Bachelot, R. Reversible Strong Coupling in Silver Nanoparticle Arrays Using Photochromic Molecules. *Nano Lett.* **2013**, *13*, 282–286.
 26. Govorov, A. O.; Zhang, W.; T., S.; Richardson, H.; Lee, J.; Kotov, N. A. Gold Nanoparticle Ensembles as Heaters and Actuators: Melting and Collective Plasmon Resonances. *Nanoscale Res. Lett.* **2006**, *1*, 84.
 27. Richardson, H. H.; Carlson, M. T.; Tandler, P. J.; Hernandez, P.; Govorov, A. O. Experimental and Theoretical Studies of Light-to-Heat Conversion and Collective Heating Effects in Metal Nanoparticle Solutions. *Nano Lett.* **2009**, *9*, 1139.
 28. Baffou, G.; Quidant, R.; Girard, C. Heat Generation in Plasmonic Nanostructures: Influence of Morphology. *Appl. Phys. Lett.* **2009**, *94*, 153109.
 29. Baffou, G.; Quidant, R.; Girard, C. Thermoplasmonics Modeling: A Green's Function Approach. *Phys. Rev. B* **2010**, *82*, 165424.
 30. Baffou, G.; Rigneault, H. Femtosecond-Pulsed Optical Heating of Gold Nanoparticles. *Phys. Rev. B* **2011**, *84*, 035415.
 31. Baffou, G.; Bon, P.; Savatier, J.; Polleux, J.; Zhu, M.; Merlin, M.; Rigneault, H.; Monneret, S. Thermal Imaging of Nanostructures by Quantitative Optical Phase Analysis. *ACS Nano* **2012**, *6*, 2452–2458.
 32. Zhao, L.; Kelly, K. L.; Schatz, G. C. The Extinction Spectra of Silver Arrays: Influence of Array Structure on Plasmon Resonance Wavelength and Width. *J. Phys. Chem. B* **2003**, *107*, 7343–7350.
 33. Bouhelier, A.; Bachelot, R.; Seo Im, J.; Wiederrecht, G. P.; Lerondel, G.; Kostcheev, S.; Royer, P. Electromagnetic Interactions in Plasmonic Nanoparticle Arrays. *J. Phys. Chem. B* **2005**, *109*, 3195–3198.
 34. Jackson, J. D. *Classical Electrodynamics*; Wiley: New York, 1999.
 35. Hohenester, U.; Trügler, A. MNPBEM - A Matlab Toolbox for the Simulation of Plasmonics Nanoparticles. *Comput. Phys. Commun.* **2012**, *183*, 370–381.
 36. García de Abajo, F. J.; Howie, A. Retarded Field Calculation of Electron Energy Loss in Inhomogeneous Dielectrics. *Phys. Rev. B* **2002**, *65*, 115418.
 37. Righini, M.; Ghenuche, P.; Cherukulappurath, S.; Myroshnychenko, V.; García de Abajo, F. J.; Quidant, R. Nano-Optical Trapping of Rayleigh Particles and Escherichia Coli Bacteria with Resonant Optical Antennas. *Nano Lett.* **2009**, *9*, 3387.
 38. Zhang, Q.; Iwakuma, N.; Sharma, P.; Moudgil, B. M.; Wu, C.; McNeill, J.; Jiang, H.; Grobmyer, S. R. Gold Nanoparticles as a Contrast Agent for *in Vivo* Tumor Imaging with Photoacoustic Tomography. *Nanotechnology* **2009**, *20*, 395102.